Analysis of the Characteristics of DC Nozzle Arcs in Air and Guidance for the Search of SF_6 Replacement Gas

J Liu[1], Q Zhang[1], J D Yan[1], J Zhong[2] and M T C Fang[1]

[1] Department of Electrical Engineering and Electronics, University of Liverpool, Brownlow Hill, Liverpool L69 3GJ, UK

[2] Henan Pinggao Group Co., Ltd. Nanhuandong Road, Pingdingshan City, 467001, China

Email: ee0u927d@liverpool.ac.uk, zhangq12@liverpool.ac.uk, yaneee@liverpool.ac.uk, zhongjy@pinggao.sgcc.com.cn and ee24@liverpool.ac.uk

Abstract. It is shown that the arc model based on laminar flow cannot predict satisfactorily the voltage of an air arc burning in a supersonic nozzle. The Prandtl mixing length model (PML) and a modified k-epsilon turbulence model (MKE) are used to introduce turbulence enhanced momentum and energy transport. Arc voltages predicted by these two turbulence models are in good agreement with experiments at the stagnation pressure (P_0) of 10 bar. The predicted arc voltages by MKE for P_0 = 13 bar and 7 bar are in better agreement with experiments than those predicted by PML. MKE is therefore a preferred turbulence model for air nozzle arc. There are two peaks in ρC_P of air at 4000 K and 7000 K due, respectively, to the dissociation of oxygen and that of nitrogen. These peaks produce corresponding peaks in turbulent thermal conductivity, which results in very broad radial temperature profile and a large arc radius. Thus, turbulence indirectly enhances axial enthalpy transport, which becomes the dominant energy transport process for the overall energy balance of the arc column at high currents. When the current reduces, turbulent thermal conduction gradually becomes dominant. The temperature dependence of ρC_P has a decisive influence on the radial temperature profile of a turbulent arc, thus the thermal interruption capability of a gas. Comparison between ρC_P for air and SF_6 shows that ρC_P for SF_6 has peaks below 4000 K. This renders a distinctive arc core and a small arc radius for turbulent SF_6, thus superior arc quenching capability. It is suggested, for the first time, that ρC_P provides guidance for the search of a replacement switching gas for SF_6.

1 Introduction

There has recently been much interest in the search of a replacement gas for SF_6 in circuit breakers since SF_6 has been shown to be a strong greenhouse gas [1]. Gas blast circuit breakers with air as an

insulation and switching medium were widely used before the introduction of SF_6 gas-blast circuit breakers [2]. At that time, there was a lack in our understanding of the physical processes occurring in air arcs due to a scarcity of reproducible experimental results of switching arcs in air. Experimental results were reported in 1970s on air arcs burning in uniform flow at constant pressure [3], in orifice flow [4] and in nozzle flow [5, 6]. However, there has been no rigorous theoretical interpretation of the experimental results reported in the aforementioned papers because of the limitation in computer power at the time and also the difficulty in accounting for radiation transport inside the arc.

Arc modelling at that time was mainly based on the integral method [5, 7-9]. This method of arc analysis has achieved considerable success in predicting the arc behaviour under steady state and for relatively high currents [5]. For switching arc applications, it is important that a theoretical arc model should be able to predict satisfactorily the arc behaviour during the current zero period. The integral method of arc analysis is not successful when applied to the current zero period due to difficulties in finding adequate correlation between the required shape factors and arc characteristic quantities [9]. Thus, arc modelling up to this time was not able to answer the question why SF_6 gas has superior arc quenching capability in gas-blast circuit breakers.

The first rigorous theoretical investigation based on arc conservation equations in laminar flow with radiation transport properly accounted for was that of Zhang et al [10] on a DC nitrogen nozzle arc at 2 kA with an upstream stagnation pressure (P_0) of 23 atm. It was shown that the arc model based on laminar flow could give satisfactory agreement between predicted and measured arc temperature, arc radius, electrical field and pressure at important locations in the nozzle. It was also shown in the study of Fang and Lin [11] that arc theory based on laminar flow could predict the critical rate of rise of recovery voltage (RRRV) within 25% of that measured for a nitrogen arc. Such an agreement is considered acceptable for circuit breakers due to the large error bar of the measured RRRV values as a result of shot to shot variation. It is therefore commonly assumed that turbulence in nitrogen or air (due to nitrogen being its major constituent) does not play a dominant role in arc extinction around current zero. However, caution must be exercised in assessing the importance of turbulence as the role of turbulence has only been tested with a single experimental case for a nitrogen nozzle arc at P_0 = 23 atm with di/dt = 36 $A\mu s^{-1}$ [11]. Thus, no firm conclusions can be drawn regarding the importance of turbulence in air or nitrogen arcs. Furthermore, no explanation could be given as regards why turbulence does not have a dominant effect on arc behavior in nitrogen around current zero.

In the search of a replacement gas for SF_6, the AC interruption capability in terms of RRRV is an essential criterion, in addition to the requirements on dielectric strength, chemical stability, toxicity, and etc. The interruption capability of air is compared with those of CO_2 and SF_6 [12]. The difference is clearly shown, however a theoretical explanation is not available, especially what material properties of a gas determine its interruption capability in nozzle flow. Without such an understanding, the search for a replacement gas with strong interruption capability will have to be undertaken by trial and error and by expensive short circuit tests.

As the first step in our effort to establish quantitative guidance on the selection of environmentally friendly switching gases, the objective of the present investigation is to establish a theoretical model for air switching arcs which can identify the dominant energy transport process responsible for the

difference in experimental arc characteristics. The material properties that are identified to be responsible for the difference in the dominant energy transport process of different gases will act as one of the guides in the search of SF_6 replacement. Since the experimental arrangement of Fang et al [5] is the closest to a switching arc, their experimental results on a DC nozzle arc in air will be used to verify the theoretical model.

The paper is organized as follows. Section 2 gives the governing equations for the arc model, the reasons for choosing the two turbulence models used in the present work and their corresponding governing equations. The computational domain and boundary conditions are presented in section 3 based on the experimental setup and conditions. In section 4, a discussion will be given on the DC arc characteristics, the dominant energy transport processes and the material properties responsible for the arc features. Finally, appropriate conclusions are drawn.

2 The governing equations and turbulence models

2.1 The governing equations

The conservation equations for an arc in local thermal equilibrium (LTE) are similar to Navier- Stokes equations but modified to take into account Lorentz force in the momentum equation, and radiation loss and electrical power input in the energy equation, which are given below:

The mass conservation equation:

$$\frac{\partial \rho}{\partial t} + \nabla \cdot \left(\rho \vec{V}\right) = 0 \tag{1}$$

The momentum conservation equation:

$$\frac{\partial}{\partial t}\left(\rho \vec{V}\right) + \nabla \cdot \left(\rho \vec{V}\,\vec{V}\right) = -\nabla \mathrm{p} + \nabla \cdot \bar{\bar{\tau}} + \vec{J} \times \vec{B} \tag{2}$$

The energy conservation equation:

$$\frac{\partial}{\partial t}(\rho e) + \nabla \cdot \left(\vec{V}(\rho e + p)\right) = \nabla \cdot \left(\mathrm{k}\nabla T + \bar{\bar{\tau}} \cdot \vec{V}\right) + \sigma \vec{E}^2 - q \tag{3}$$

In the above equations, t is the time, ρ the density, $\vec{V}$ the velocity vector, p the pressure, $\vec{J}$ the current density, $\vec{B}$ the magnetic flux density, $\vec{E}$ the electric field, T the temperature, q the net radiation loss, and e is given by

$$e = h - \frac{p}{\rho} + \frac{V^2}{2} \tag{4}$$

where h is the enthalpy which is determined by T and p in tabulated form taken from Yos [13]. T is solved by (3). $\bar{\bar{\tau}}$ in (2) and (3) is the stress tensor which is given by

$$\bar{\bar{\tau}} = (\mu_l + \mu_t)\left[\left(\nabla \vec{V} + \nabla \vec{V}^T\right) - \frac{2}{3}\nabla \cdot \vec{V} I\right] \tag{5}$$

where I is an identity matrix and μ the viscosity. The subscripts l and t represent, respectively, the molecular and turbulent part of the viscosity.

In the present work, the arc and its surrounding gas are assumed to be axisymmetric, and the axial and radial velocity components are respectively denoted by w and v. This assumption is based on the fact that the nozzle arrangement used in the experiment is axisymmetric. For arcs in laminar flow, the eddy

viscosity, μ_t, and turbulent thermal conductivity, k_t, are set to zero. For turbulent flow, the above equations are time averaged. The determination of μ_t and k_t is deferred to Section 2.2.

Since the publication of the thermodynamic and transport properties of air by Yos in 1967 [13] and by Deveto in in 1976 [14], there had been little activities in this area for nearly 20 years. There was a surge of activities in the calculation of high temperature air plasma properties due to its applications in thermal plasmas firstly by Murphy in 1995 [15] and then followed by the groups headed by Capitelli, e.g. [16] and Gleizes, e.g. [17, 18] and, most recently, by Wang et al [19]. The most important transport property for turbulent arc modelling is the electrical conductivity. A comparison of electrical conductivity given in the aforementioned papers with the experimental results of Asinovsky et al [20] and of Schreiber et al [21] has been performed (reported in [22]), which shows a preference for the use of Yos 1967 data [13]. In addition, there is an excellent agreement between the measured arc conductance of an AC air wall-stabilized arc column and the computational results using Yos data [23]. Thus, for the present investigation, thermodynamic and transport properties of air as a function of pressure and temperature are taken from Yos [13].

Ohm's law reads

$$\vec{J} = \sigma\vec{E} \tag{6}$$

where σ is the electrical conductivity. $\vec{E}$ can be calculated in two ways. An arc in a supersonic nozzle is similar to a boundary layer [24]. Thus, the axial component of $\vec{E}$, E_z, is uniform across an arc cross section and the radial component of the $\vec{E}$, E_r, is negligible [7, 24]. The axial component of $\vec{E}$ can therefore be calculated by

$$E = E_z = \frac{i}{\int_0^\infty \sigma 2\pi r dr} \tag{7}$$

Equation (7) is known as the slender arc model [24]. The integration in equation (7) stops at the radial position where temperature is 4000 K, at which σ is 3 orders of magnitudes less than that above 8000 K [13]. With an increasing current, the radial extent of the arc is no longer much smaller than the arc length. The slender arc model is no longer applicable [24]. $\vec{E}$ is then calculated via electrical potential, φ, using the current continuity equation:

$$\nabla \cdot (\sigma \nabla \varphi) = 0 \tag{8}$$

The axial and radial components of $\vec{E}$ are given by

$$E_z = -\frac{\partial \varphi}{\partial z} \; and \; E_r = -\frac{\partial \varphi}{\partial r} \tag{9}$$

For axisymmetric arc, the azimuthal magnetic flux density can be calculated by

$$\mathrm{B}_\theta = \frac{\mu_0 \int_0^r j_z 2\pi\xi d\xi}{2\pi r} \tag{10}$$

where j_z is the axial component of the current density and μ_0 the permeability of free space. The two components of Lorentz force are given by

$$f_r = -j_z \mathrm{B}_\theta \; and \; f_z = j_r \mathrm{B}_\theta \tag{11}$$

The approximate radiation transport model of Zhang et al [10] is adopted to calculate the net radiation loss in the energy equation. In the arc core, the boundary of which is defined at the point of 83% of the

axis temperature, *q* in the energy conservation equation is equal to the net emission coefficient (NEC), which is a function of the local pressure, temperature and the arc's radiation radius. This radiation radius is defined as $0.5(R_{83}+R_{4K})$, where R_{83} is the radius of the boundary of the high temperature arc core (hereafter referred to as the core boundary, which is define as the isotherm of 83% of the axis temperature) and R_{4K} the radius of the electric boundary (defined as 4000 K isotherm) [24]. NECs for air differ widely depending on the authors [25-29]. The disagreement of the NEC data by different authors are due to the differences in the spectra data used for the calculation of the spectral absorption coefficients and also the atomic and molecular data required for the computation of plasma composition. No experimental results for air are available for the verification of theoretically derived NEC. It is therefore not possible to judge the relative merits of the spectral data used by different authors [25-29]. When radiation absorption is important, the NECs for air and nitrogen are close to each other even for a very small arc of 1 mm in radius [25, 26, 28, 30]. This indicates that, for practical purposes, NEC for nitrogen can be used for air. The experimentally derived nitrogen NEC of Ernst et al [31] can be used to compare with those computed NEC by Shayler and Fang [32], Aubrecht and Bartlova [25] and Gleizes et al [30]. The NEC of Shayler and Fang [32] is the closest to that of Ernst et al [31] but it is still on average lower than the latter by a factor of 2. We therefore use the NEC for nitrogen given in [32] but multiplied by a factor of 2 to compute the radiation loss in the arc core of an air nozzle arc. Radiation flux at the core boundary will be absorbed in a region where the temperature decays to ambient. It is assumed that 60% of the radiation flux at the core boundary is absorbed in the region between the core boundary and the 4000 K isotherm [10]. This is consistent with the estimated radiation loss of an air arc [4].

2.2 Flow models

There has been no firm conclusion on whether turbulence is important for DC air nozzle arcs. The ultimate approach to establish the role of turbulence is by comparison between experimental results and those predicted by an arc model based on laminar flow assumption (hereafter referred to as the laminar flow model). If such a comparison is not satisfactory, we investigate the arc behaviour under turbulent flow conditions. This approach is justified in that, under the same pressure difference across the nozzle, an air arc can attain a much higher velocity than that of an SF_6 arc. An air arc is therefore more likely to be in turbulent state than an SF_6 arc because of its higher Reynolds number. The influence of turbulence generated by shear layer instability on SF_6 nozzle arcs is well established (e.g. [33]). In addition, voltage oscillations induced by turbulent motion of an air arc column in a gas-blast circuit breaker has been experimentally observed [34].

The flow inside a nozzle is dominated by its axial velocity component with a large radial gradient, which typifies a shear layer flow [35]. Of the turbulence models dealing with shear layer flow [36, 37], two turbulence models, the Prandtl mixing length model and the standard k-epsilon model, have been shown, in comparison with other turbulence models [33, 38], to be the most appropriate for turbulent nozzle arcs. Thus, these two turbulence models will be applied to the air arc if the laminar flow model fails to give satisfactory agreement with the experimental results of [5]. For completeness and for the ease of reference, the relevant equations for these two turbulence models are given below.

2.2.1 The Prandtl mixing length model

For this model, the eddy viscosity, μ_t, is computed by

$$\mu_t = \rho \lambda_c V_c \tag{12}$$

where λ_c is the mixing length, i.e. the turbulence length scale, which is related to the thermal radius r_δ by

$$\lambda_c = c r_\delta \tag{13}$$

where c the turbulence parameter, the value of which is to be found by matching the predicted arc voltage with one measured voltage and

$$r_\delta = \sqrt{\int_0^\infty \left(1 - \frac{T_\infty}{T}\right) 2r dr} \tag{14}$$

where T_∞ is defined in [38]. The velocity scale defined in the Prandtl mixing length model is given by

$$V_c = \lambda_c \left(\left| \frac{\partial w}{\partial r} \right| + \left| \frac{\partial v}{\partial z} \right| \right) \tag{15}$$

2.2.2 Standard k-epsilon model

The standard k-epsilon model computes the length and velocity scales of turbulence, and thus the eddy viscosity, based on two partial differential equations, one of which for the turbulent kinetic energy per unit mass, k, and the other for the turbulence dissipation rate, ε. The corresponding governing equations are given below

$$\frac{\partial}{\partial t}(\rho k) + \nabla \cdot \left(\rho k \vec{V}\right) = \nabla \cdot \left(\left(\mu_l + \frac{\mu_t}{\sigma_k}\right) \nabla k \right) + G_k - \rho \varepsilon \tag{16}$$

$$\frac{\partial}{\partial t}(\rho \varepsilon) + \nabla \cdot \left(\rho \varepsilon \vec{V}\right) = \nabla \cdot \left(\left(\mu_l + \frac{\mu_t}{\sigma_\varepsilon}\right) \nabla \varepsilon \right) + C_{1\varepsilon} G_k \frac{\varepsilon}{k} + C_{2\varepsilon} \rho \frac{\varepsilon^2}{k} \tag{17}$$

where G_k is the generation rate of the turbulence kinetic energy which is given for axisymmetric arc by

$$G_k = \mu_t \left[2\left(\frac{\partial w}{\partial z}\right)^2 + 2\left(\frac{\partial v}{\partial r}\right)^2 + 2\left(\frac{v}{r}\right)^2 + \left(\frac{\partial w}{\partial r} + \frac{\partial v}{\partial z}\right)^2 \right] \tag{18}$$

The length and velocity scales of turbulence are respectively defined as

$$\lambda_c = C_u \frac{k^{1.5}}{\varepsilon} \; and \; V_c = \sqrt{k} \tag{19}$$

and the eddy viscosity is given by

$$\mu_t = \rho C_u \frac{k^2}{\varepsilon} \tag{20}$$

The default values of the turbulence parameters for the standard k-epsilon model are: $\sigma_k = 1.0$, $\sigma_\varepsilon = 1.3$, $C_{1\varepsilon} = 1.44$, $C_{2\varepsilon} = 1.92$ and $C_u = 0.09$.

In the energy equation, turbulent thermal conductivity is related to eddy viscosity through the turbulence Prandtl number, Pr_t :

$$k_t = \frac{C_p \mu_t}{Pr_t} \tag{21}$$

where $Pr_t = 1$ [33].

3 Computational domain and boundary conditions

Computation has been performed for the Teflon nozzle of Fang et al [5] using the parallel processing facilities of ANSYS Fluent [39]. The computation domain and the grid system are shown in figure 1 where the detailed dimensions and the distribution of grids are given. Tests with different grid size have been conducted to ensure that the grids are sufficiently fine to attain satisfactory computational accuracy. The arc length is 100 mm with the downstream electrode tip located 10 mm away from the nozzle exit (not shown in the diagram). For all discharge conditions reported in [5], the exit pressure (1 bar) is low enough to ensure that the flow in the nozzle is supersonic and shock free.

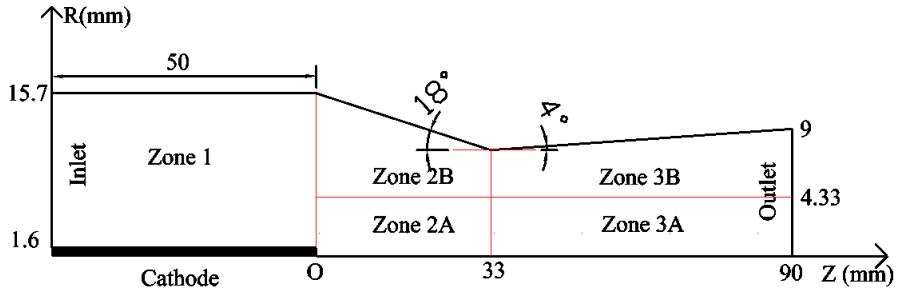

Figure 1. Nozzle geometry (not to scale) and grid system. The computation domain is divided into 5 zones: In Zone 1: a non-structured grids consisting of triangle cells with an average edge size of 0.5 mm is used. There are altogether 6872 grids. In Zone 2A uniform rectangular grids are used with a total number of grids of 66 (axial) x 130 (radial). There are 66 x 30 grids in Zone 2B. A total of 114 x 130 rectangular grids are placed in Zone 3A and 114 x 30 grids in Zone 3B. The radius of upstream electrode is 1.6mm. The radius of nozzle throat is 5mm. The origin of z-axis is at the upstream electrode tip.

Computation has also been done to include the downstream electrode with an open boundary sufficiently far from the downstream electrode (known as the extended domain) to simulate the exhaust space for discharging the gas from the nozzle. The results inside the nozzle using the extended domain are the same as the arc computed for the domain given in figure 1. For the case with downstream electrode included in the computation domain, electrical field between the nozzle exit and the tip of the downstream electrode is smaller than that at the nozzle exit due to the enlarged arc size when axial velocity is slowed down to zero at the downstream electrode surface (figure 9(b)). Thus, the use of the electrical field at the nozzle exit to calculate the voltage drop in the arc section between nozzle exit and the downstream electrode tip tends to overestimate the arc voltage. For the current range investigated, the overestimation of arc voltage is less than 2% of the total arc voltage. This is much smaller than the measurement error of arc voltage of about $\pm$10% caused by shot to shot variation (figure 8). Since the focus of the current investigation is the study of the properties of arc column, we use the computation domain given in figure 1 to save computation time.

The boundary conditions for the arc conservation equations and the governing equations for the k-epsilon turbulence model are given in table 1. When the current is around 2 kA and above at a stagnation pressure of 10 bar, the arc fills the nozzle near the exit. We use the non-slender arc model to check if in this region the electrical field can still be calculated by using the slender arc model. The computation domain for electric field is extended in the radial direction to 60 mm from the axis since electrical field is a long range force. The boundary conditions for equation (8) are given below:

(a) The current density entering upstream electrode at the nozzle entrance is assumed uniform.

$$j_z = -\sigma\frac{\partial\varphi}{\partial z} = \frac{i}{A_{electrode}} \quad (22)$$

where $A_{electrode}$ is the cross-sectional area of the upstream electrode.

(b) At the nozzle exit plane, the electrical potential is set to zero, i.e. $\varphi = 0$.

(c) At all the other boundaries of the computational domain, including the axisymmetric axis, the normal gradients of the electrical potential are set to zero.

Table 1. Boundary conditions for the arc conservation equations and the equations describing *k and ε*

Nozzle axis	Axisymmetrical boundary conditions are applied. Thus, all radial derivatives of the dependent variables are set to zero except for the radial velocity which is zero on the axis.
Nozzle inlet	Pressure inlet boundary conditions supplied by ANSYS Fluent [39] are used. Axial velocity and density are iteratively computed according to the calculated inlet static pressure by assuming that the gas entering the nozzle undergoes an isentropic process [33] from a reservoir with stagnation pressure P_0 and stagnation temperature T_0 (300 K).
Nozzle exit	Pressure outlet boundary conditions supplied by ANSYS Fluent [39] are used. Exit static pressure, P_e, need to be specified. During computation, if the flow is supersonic at the flow exit, the setting of P_e will be ignored and gas pressure, velocity and temperature at exit are extrapolated from upstream assuming zero gradient of a dependent variable at the exit plane. If the flow is subsonic at the nozzle exit, P_e is the exit pressure.
Other solid surfaces (nozzle wall and electrode surface)	Non-slip boundary condition for velocity is applied through a built-in wall function of ANSYS Fluent [39]. These surfaces are assumed to be adiabatic, for which the heat flux is set to zero.
Boundary conditions for the k-epsilon turbulence model	Nozzle inlet: *k* and *ε* are given by [33] $k_{in} = \frac{3}{2}(u_{in}I_t)^2$ $\varepsilon_{in} = C_\mu^{3/4}\frac{k_{in}^{3/2}}{l}$ where u_{in} is the nozzle inlet velocity, I_t the turbulent intensity set at 5% and l=0.07L [33]. L is the characteristic length of the equipment [33] given by (d_{inlet} - $d_{electrode}$) where d_{inlet} is the diameter of the nozzle inlet and $d_{electrode}$ the electrode diameter. Nozzle outlet: the axial gradients of *k* and *ε* are set to zero.

4 Results and discussion

Computation has been carried out for 3 stagnation pressures (P_0 = 13 bar, 10 bar and 7 bar) and for DC currents from 250 A to 3 kA. The voltage computed by the laminar flow model is considerably lower than that measured (figure 8). The differences between the predicted and measured arc voltages, especially towards the low current end, are well beyond the ±10% experimental uncertainty [5] due to shot to shot variation. In addition, considerations of the effects of departure from LTE [40-42] inside an arc in laminar flow result in the prediction of poorer interruption than that of an LTE arc in laminar

flow. It is well-known that reaction rates are greatly enhanced under turbulent conditions [43]. We therefore adopt a turbulent LTE arc model. In view of the fact that there is no ready turbulence model that can predict turbulent effects accurately with universal turbulence parameters, suitable level of turbulence is then added to the flow by calibrating the turbulence parameters. The Prandtl mixing length turbulence model and the k-epsilon model are used to account for the turbulence enhanced momentum and energy transport. The turbulence parameter, *c*, in the Prandtl mixing length model (hereafter referred to as PML) is adjusted to give the closest agreement with the measured arc voltage at 1 kA DC and P_0=10 bar. *c* has been found equal to 0.06.

Arc voltages predicted by the k-epsilon model with the default values of the 5 turbulence parameters (hereafter referred to as the standard k-epsilon model) are considerably higher than those measured, especially at low currents (figure 8). This indicates turbulence effects are too strong. Similar results were obtained when this turbulence model is applied to a round turbulent jet [44]. To reduce turbulence effects, we increase the production of turbulence dissipation by adjusting the value of $C_{1\varepsilon}$ in equation (17) to match the predicted arc voltage with that measured at 1 kA DC and P_0=10 bar. The value of $C_{1\varepsilon}$ has been found to be 1.62. It is evident from figure 8 that the calibrated turbulence models lead to satisfactory prediction of the arc voltage over the whole current range. $C_{1\varepsilon} = 1.62$ and c = 0.06 have therefore been used to compute the arc voltage for other discharge conditions reported in this paper. We refer to the k-epsilon model with the modified value of $C_{1\varepsilon}$ as the modified k-epsilon model, or MKE for easy reference.

Computational results are presented for the laminar flow model, PML and MKE (known collectively as the flow models for future reference). The inclusion of the laminar flow model is to illustrate the difference between arc characteristics in laminar and turbulent flows. Since the standard k-epsilon model is the most commonly used turbulence model, its results will be presented to show its over-prediction of turbulence effects. The qualitative features of the computational results are similar for different stagnation pressures. Unless otherwise specified, the computational results obtained for P_0 = 10 bar are used for discussions.

4.1 Features of arc-flow interaction

Figure 2 shows the temperature field together with the pressure isobars computed by the three flow models for a 2 kA DC arc at P_0 = 10 bar. There is a distinctive core structure, which is surrounded by cold gas (figure 2(a)), for the arc in laminar flow. The corresponding mass flow rate is approximately 65% of that of the cold flow case (i.e. in the absence of an arc) which is 0.187 kgs^{-1}. It is noted that turbulence has little effects on the cold flow. The arc size represented by the position of the 4000 K isotherm (hereafter referred to as the arc radius or electrical boundary) is the smallest for arc in laminar flow and the largest for PML as shown in figure 3. At the nozzle exit, the surrounding cold gas has almost disappeared for PML (Curve (2), figure 3). Further increase in current will result in the arc electrical boundary touching the Teflon nozzle surface for PML. Under these circumstances, nozzle ablation may need to be taken into account. However, it would be shown later that the estimated power into the nozzle surface in the section where arc touches the nozzle wall will not cause ablation in the time duration during which the experiments were conducted [5]. For MKE, there is still a distinctive layer of cold flow surrounding the arc at 2 kA (Curve (3), figure 3). The mass flow rates for PML and MKE are respectively 26% and 32% of the cold flow case. Compared with the arc in laminar flow, the

much reduced mass flow rate for PML and MKE is due to the spread of arc thermal influence region by turbulence. Therefore, the presence of an arc reduces the effective flow area inside the nozzle, thus modifying the pressure distribution in the nozzle, which in turn affects the arc. Such modification is shown in figure 4(a) for the axis pressure distributions of the three flow models together with that of the cold flow. For the cold nozzle flow, axis pressure shows a rapid pressure drop in the vicinity of the nozzle throat (thus strong gas acceleration), but rather gentle pressure variation in a large part of the diverging section. The presence of the 2 kA DC arc results in an increase in pressure but a reduction in its gradient in comparison with that of cold flow. The distributions of axis pressure (figure 4(a)) and axis velocity (figure 4(b)) for PML and MKE start to diverge from each other just before the nozzle throat, where the flow starts to accelerate rapidly. The turbulence effects produced by MKE are stronger than that of PML, which results in lower flow acceleration, hence a smaller pressure gradient. Thus, the axis pressure of MKE is higher than that of PML. Velocity field is closely coupled with the temperature field, the close interaction of which determines voltage-current (V-I) characteristics. This is discussed in Section 4.2.1.

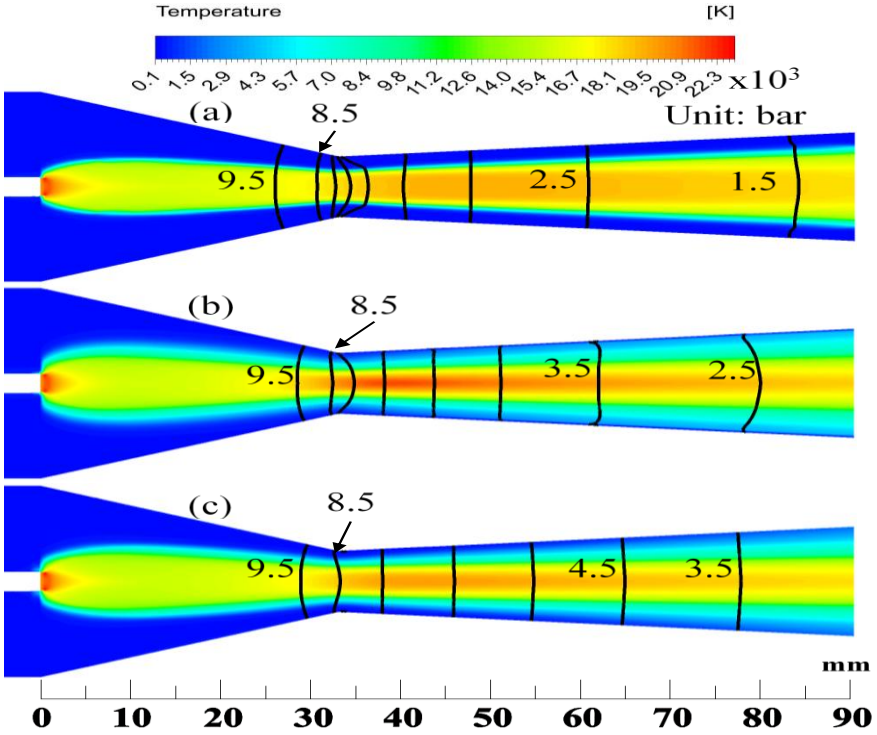

Figure 2. Temperature contour together with pressure isobars for a 2 kA DC arc at P_0 = 10 bar computed by (a) laminar flow model, (b) PML and (c) MKE. The pressure difference between two adjacent isobars is 1bar.

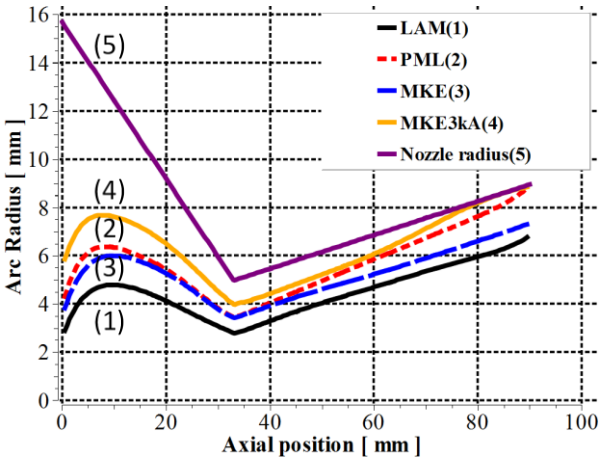

Figure 3. Variations of arc radius (radial position of 4000 K isotherm) for the 2 kA case computed by (1) laminar flow model; (2) PML and (3) MKE. Curve (4) is the arc radius for 3 kA computed by MKE, which shows that near the nozzle exit hot gas occupies the whole nozzle. Nozzle radius (5) is plotted to show the arc size in relation to the nozzle.

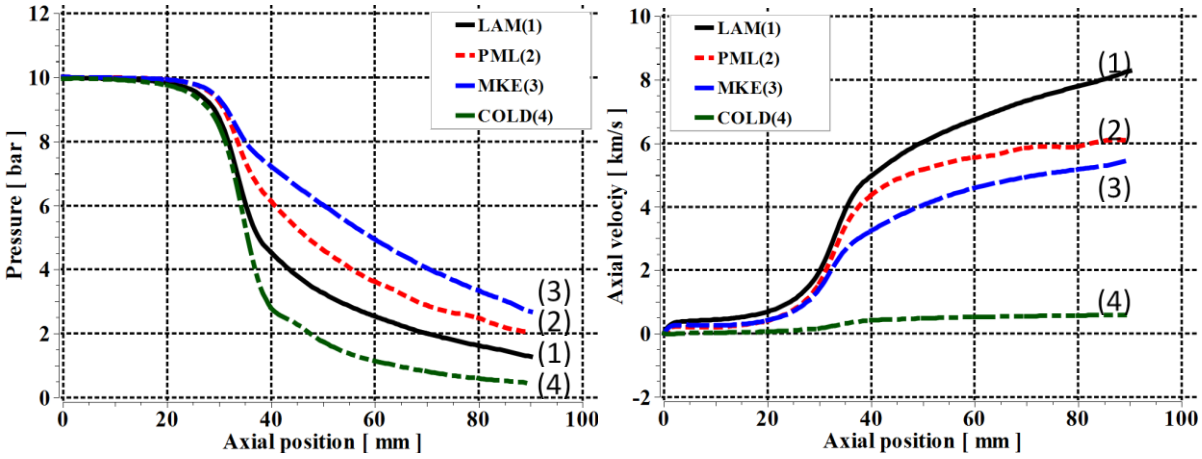

(a) (b)

Figure 4. Variations of (a) pressure and (b) axial velocity along the nozzle axis for the 2 kA DC arc computed by the three flow models. The pressure and axial velocity for the cold flow (Curve (4)) are also plotted to show the effects of the presence of the 2 kA DC arc.

When current is reduced to 1 kA, the qualitative features of the steady state arc predicted by the three flow models are similar to those of the 2 kA arc. With further decrease in current the arc core shrinks and the mass flow rate passing the nozzle increases. At 250 A (figure 5), the mass flow rate has attained 93% of the cold flow in the laminar case and 80% for MKE and PML. There is very little difference between the aerodynamic features in terms of axis pressure (figure 6(a)) and axis velocity (figure 6(b)) for the two arcs predicted by MKE and PML. In contrast with the 2 kA case, the axis velocity in the divergent section of the nozzle at 250 A no longer increases with distance for both turbulence models. This is due to the increased turbulence intensity when current is reduced as well as due to the axial development of turbulence level along the nozzle length for a given current (figure 7). In the vicinity of the throat where flow is accelerated rapidly, turbulent kinetic energy, *k*, reaches a maximum for 250 A. The subsequent decay of *k* is due to a drop in axial velocity component as a consequence of turbulent momentum diffusion. The decrease in axial velocity and the axial expansion

of arc size result in a decrease of the rate of turbulence production for 250 A (equation (18)), hence the reduction of *k* towards the nozzle exit. For the 2 kA arc, the monotonic increase of *k* is attributed to the continuous flow acceleration (figure 4(b) and 7).

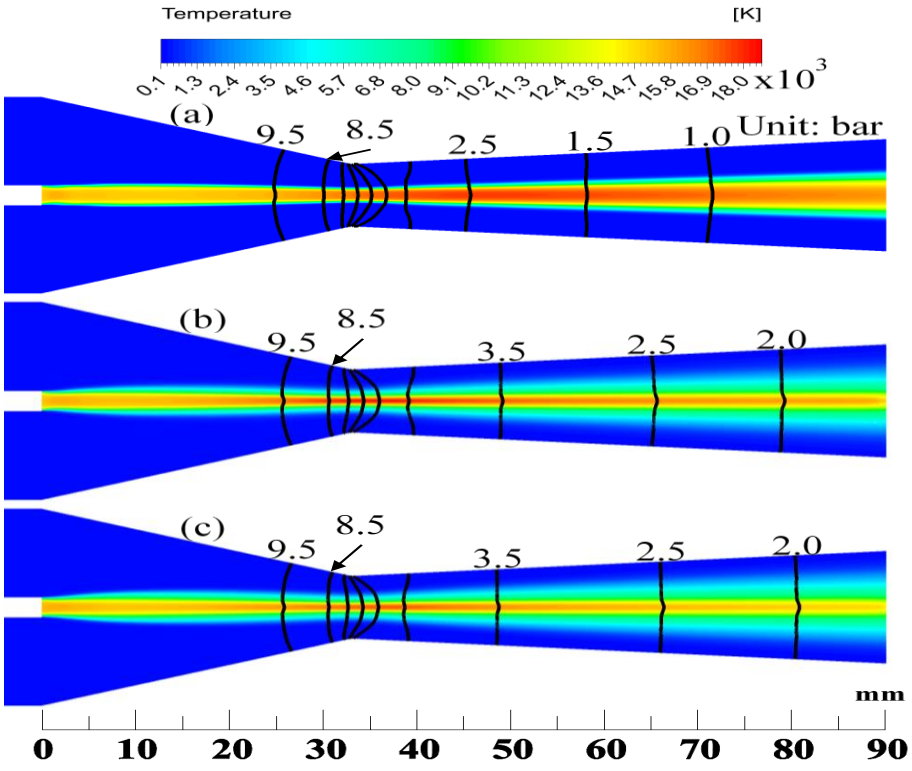

Figure 5. Temperature contour together with pressure isobars for a 250 A DC arc at P_0 = 10 bar computed by (a) laminar flow model, (b) PML and (c) MKE. The pressure difference between two adjacent unlabelled isobars after 8.5 bar is 1 bar.

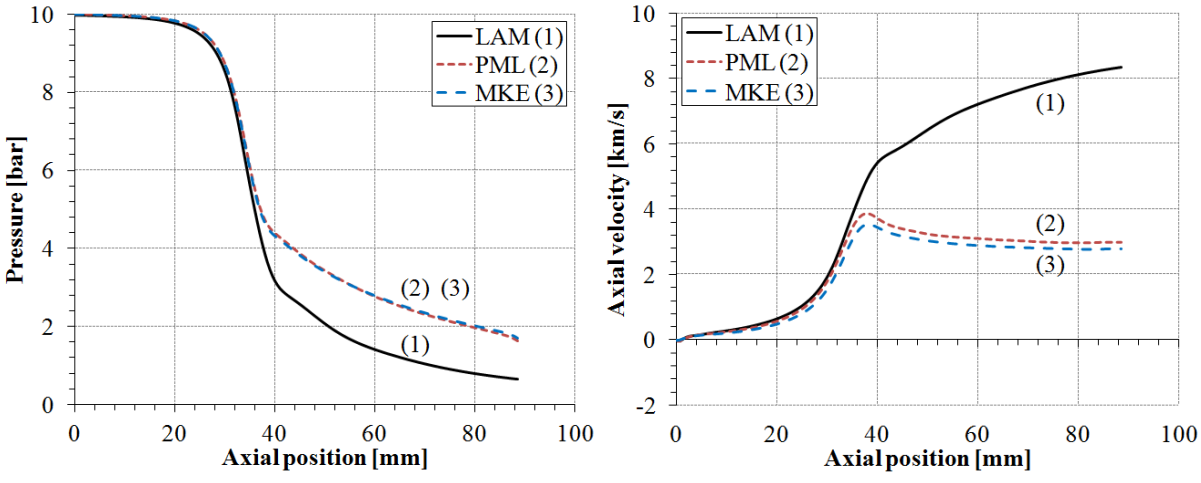

(a) (b)

Figure 6. Variations of (a) pressure and (b) axial velocity along the nozzle axis for the 250 A DC arc computed by the three flow models.

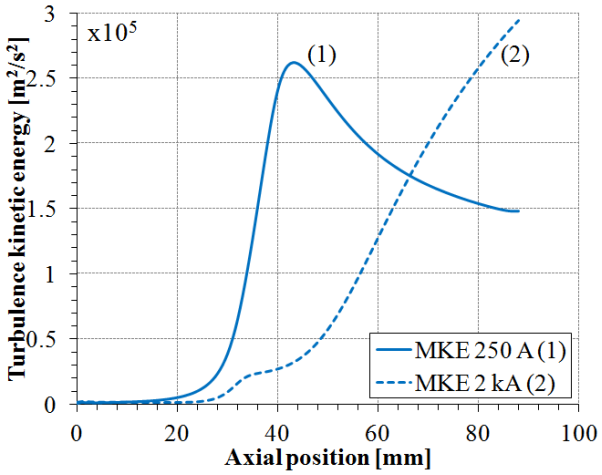

Figure 7. Variation of turbulence kinetic energy per unit mass, *k*, along the nozzle axis: (1) 250 A and (2) 2 kA calculated by MKE.

4.2 Characteristics of DC nozzle arcs

4.2.1 DC Voltage-Current (V-I) characteristics

The DC V-I characteristics of the air nozzle arcs have been computed using the three flow models. The computed arc voltages are plotted in figure 8 together with the experimental results given in [5] for comparison. The measured and computed arc voltages show a flat part of the V-I characteristic at currents above 1.5 kA and a negative V-I characteristic for currents below 1.5 kA. Comparison between measured and computed arc voltages shows that the arc voltage predicted by the laminar flow model is lower than that measured, especially at lower currents. The standard k-epsilon model, PML and MKE give good agreement for currents at 2 kA and above with the standard k-epsilon model grossly over predicting the arc voltage at low currents. Voltage computed by PML is about 10% lower than the corresponding experimental result at 250 A, the lowest current for which experimental results are available for comparison. Such a difference is well within experimental error. Overall, MKE gives the best agreement with the measured voltage. The physical processes responsible for such V-I characteristics are discussed in the following two subsections.

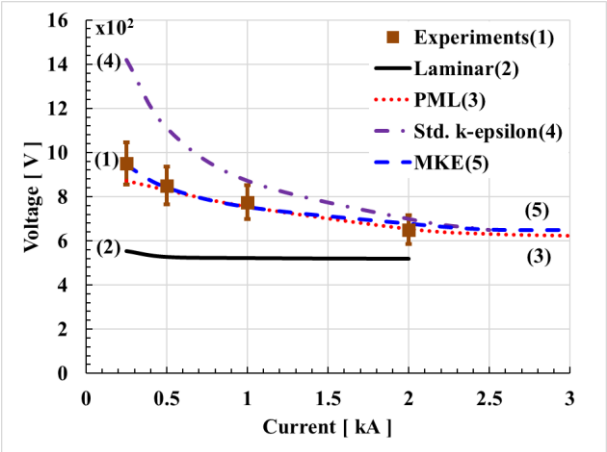

Figure 8. V-I characteristics for the DC air nozzle arcs at P_0=10 bar computed by the three flow models. Experimental error of ±10% around the mean value is due to shot to shot variation [5].

4.2.2 *Characteristics of nozzle air arc with radiation dominated arc core*

A. Overall features

V-I characteristics are determined by the electrical conductance of the arc which is in turn dependent on the temperature distribution within the arc. The temperature field is a result of energy balance between power input and various energy transport processes as described by the energy conservation equation. Attention will be paid to identify the dominant energy transport process.

Examination of the computational results for the flat part of the V-I characteristics, given by the three flow models, shows that the axis temperature for currents of 2 kA and above is not sensitive to the current for a given arc model (e.g. Curves (3) and (4) in figure 9(a)). The arc radius is approximately proportional to the square root of current (figure 3) for the part of the nozzle where arc is surrounded by a cold layer of gas flow (figure 3). Thus, the local arc conductance becomes proportional to arc current. The electric field distribution is not sensitive to the current for a given arc model (figure 9(b)) and the arc voltage is almost independent of current (figure 8).

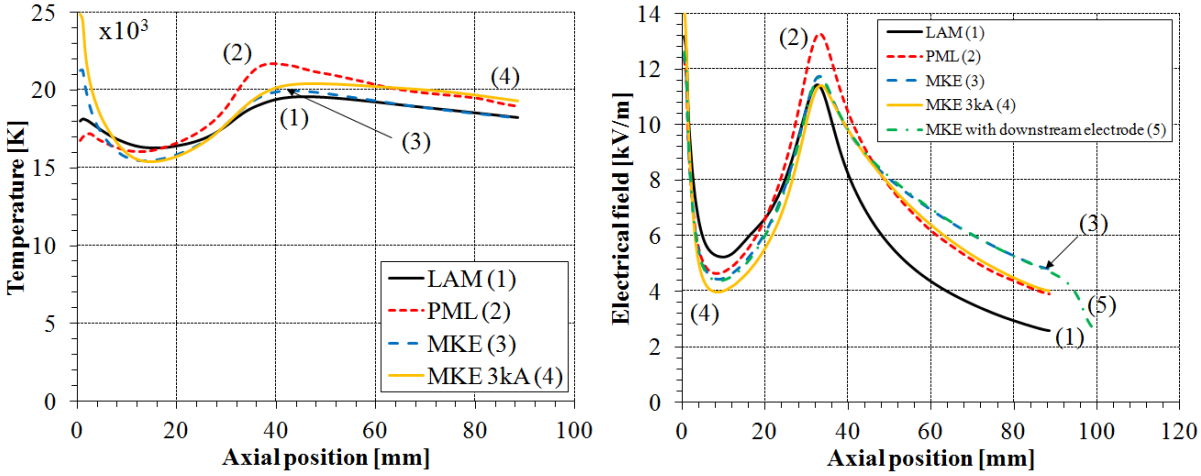

(a) (b)

Figure 9. Variations of (a) axis temperature and (b) electrical field of the 2 kA arc computed by the three flow models. The axis temperature and electrical field of a 3 kA arc obtained by MKE are also plotted for comparison. Curve (5) in (b) is the electrical field computed by MKE with downstream electrode included. Curves (3) and (5) are identical up to the nozzle exit at 90 mm.

As previously noted, the divergent angle of the nozzle in figure 1 is very small. At 3 kA with adiabatic boundary condition for temperature, the temperature near the wall is over 4000 K in the region within 10 mm to the nozzle exit. Radiation loss which escapes from the arc near the nozzle exit at 3 kA is less than 15% of local Ohmic input. Radiation induced Teflon ablation is unlikely as at this power level (approximately 2 x 10^6 W/m with the exit electrical field given in figure 9(b)) Teflon will not reach its melting point for the experimental duration of 7 ms [45]. The measured arc voltage at 3 kA (figure 8) remains the same as that of 2 kA within experimental error, which indicates that ablation is unlikely to take place. However, it should be noted that 3 kA should be considered as the upper current limit for the validity of adiabatic boundary condition for the nozzle in figure 1.

At 2 kA, the arc thermal influence region extends close to the wall (figures 2 and 3) for the two turbulence models. The arc can no longer be considered as slender in the sense of a boundary layer. We therefore solve the current continuity equation (equation (8)) for electrical potential with an enlarged computation domain, the results of which are shown in figure 10. Equipotential lines are almost perpendicular to the nozzle axis indicating that radial component of electrical field is negligible and the axial component is uniform across an arc cross section. Thus, simplified Ohm's law (equation (7)) is used to compute the axial electrical field for currents less than 2 kA.

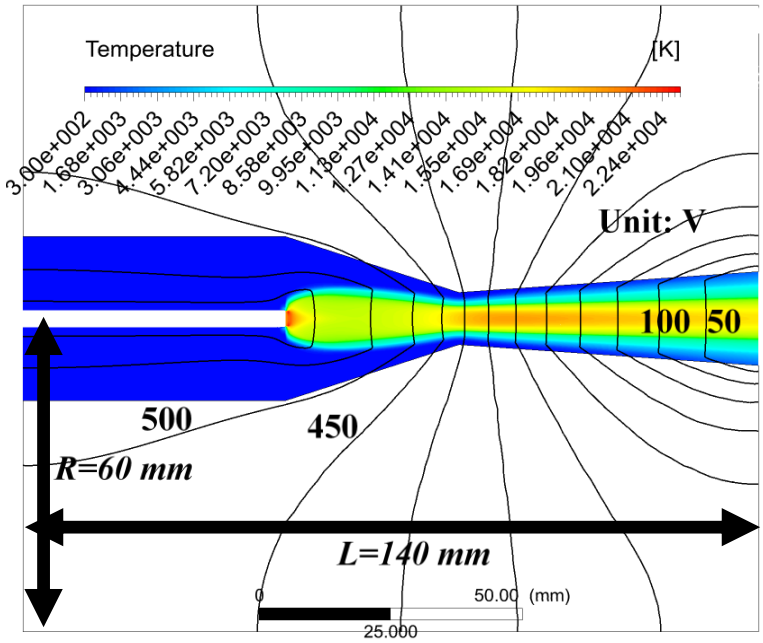

Figure 10. Temperature contour together with equipotential lines for the 2 kA DC arc at P_0 = 10 bar computed by MKE. Potential difference between two adjacent equipotential lines is 50 V. Computation domain has been extended to a radius of 60 mm from the axis to ensure that the potential distribution is no longer affected the size of the computation domain.

B. Distinctive features of radial temperature profiles and the influence of material properties

Of the three flow models, the arc in laminar flow shows a distinctive high temperature core (figure 2) which results in the smallest arc radius. As radial temperature profile determines the local electrical field, it would be interesting to see the features of the radial temperature profiles predicted by the three flow models. In figure 11, the radial temperature profiles at three typical axial stations, the upstream midsection, the nozzle throat and the downstream midsection are plotted.

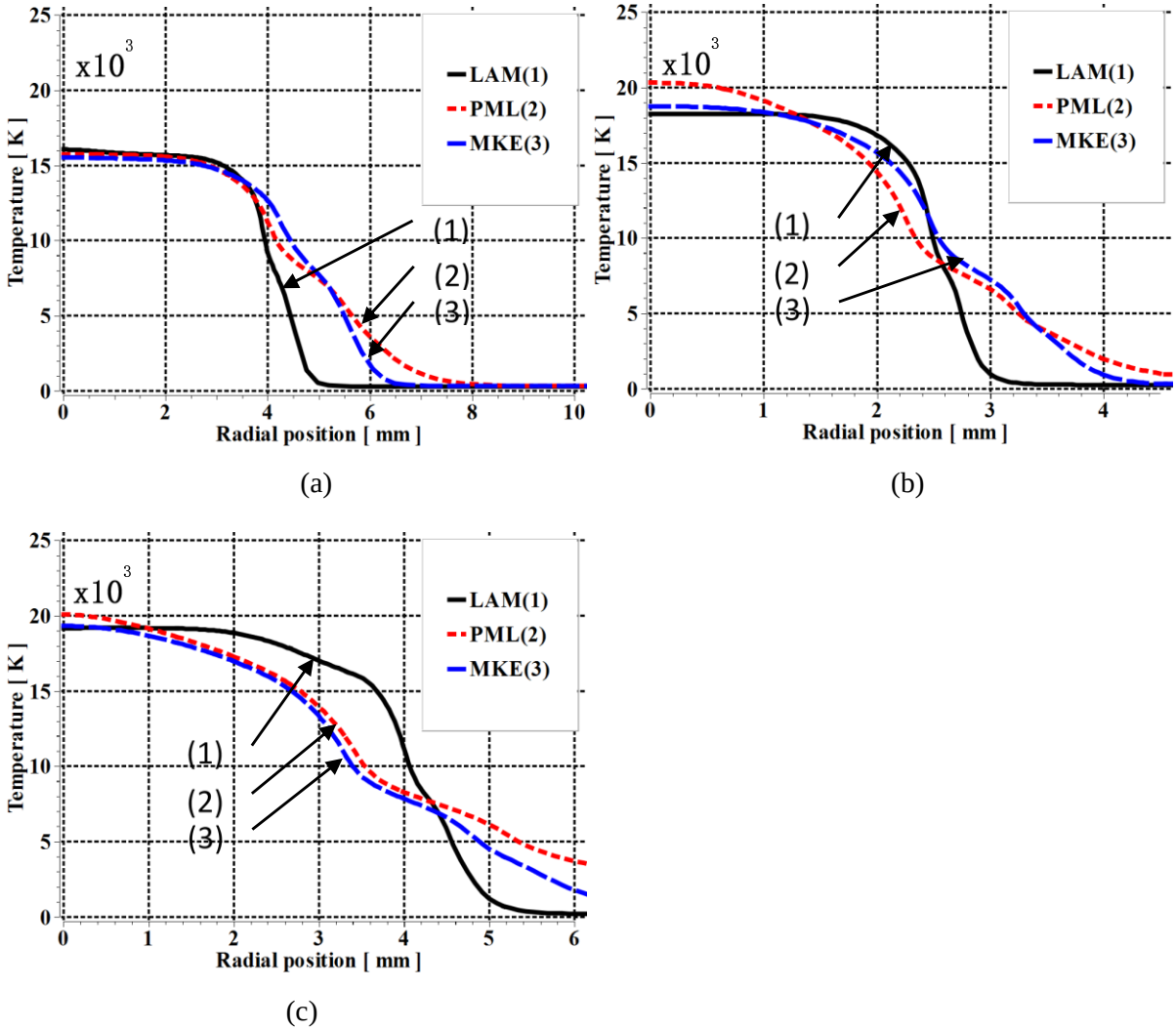

Figure 11. Radial temperature profiles computed by the three flow models for the 2 kA DC arc at P_0 = 10 bar. (a) Upstream midsection z= 15 mm, (b) Nozzle throat, z= 33 mm and (c) Downstream midsection z= 60 mm.

In the arc core, temperature is almost constant for the arc in laminar flow, but for PML and MKE, the effects of turbulence enhanced thermal conduction are clearly shown in the region downstream of nozzle throat (figure 11(c)). However, for all the three flow models, radiation transport is the dominant energy transport process. In the radiation re-absorption region where 60% of radiation at the core boundary is absorbed, the thickness of this region and the slope of the temperature profile differ greatly depending on the flow model. There are several inflection points on the radial temperature profiles predicted by PML and MKE which correspond to the peaks of effective thermal conductivity (figure 12). One inflection point is at approximately 7000 K and the other around 4000 K. The temperature gradient is mainly determined by the thermal conductivity. The molecular thermal conductivity for the laminar arc is much smaller than the effective turbulent thermal conductivity (figure 12), which is the sum of molecular and turbulent thermal conductivity. This explains why the temperature gradient in the radiation absorption region of the laminar arc is the largest, thus a thin radiation re-absorption region. Because of the large effective thermal conductivity at the nozzle throat and in the divergent section of the nozzle (figure 12(b) and (c)), the thickness of the radiation

re-absorption region is much bigger than that of the laminar case.

The effective thermal conductivity has rather complex features (figure 12). Since turbulent thermal conductivity is the dominant component of effective thermal conductivity, we examine the features of eddy kinematic viscosity. Effective thermal conductivity is the product of effective eddy kinematic viscosity with the material property, ρC_P. Radial profiles of effective kinematic viscosity for the 2 kA arc are given in figure 13.

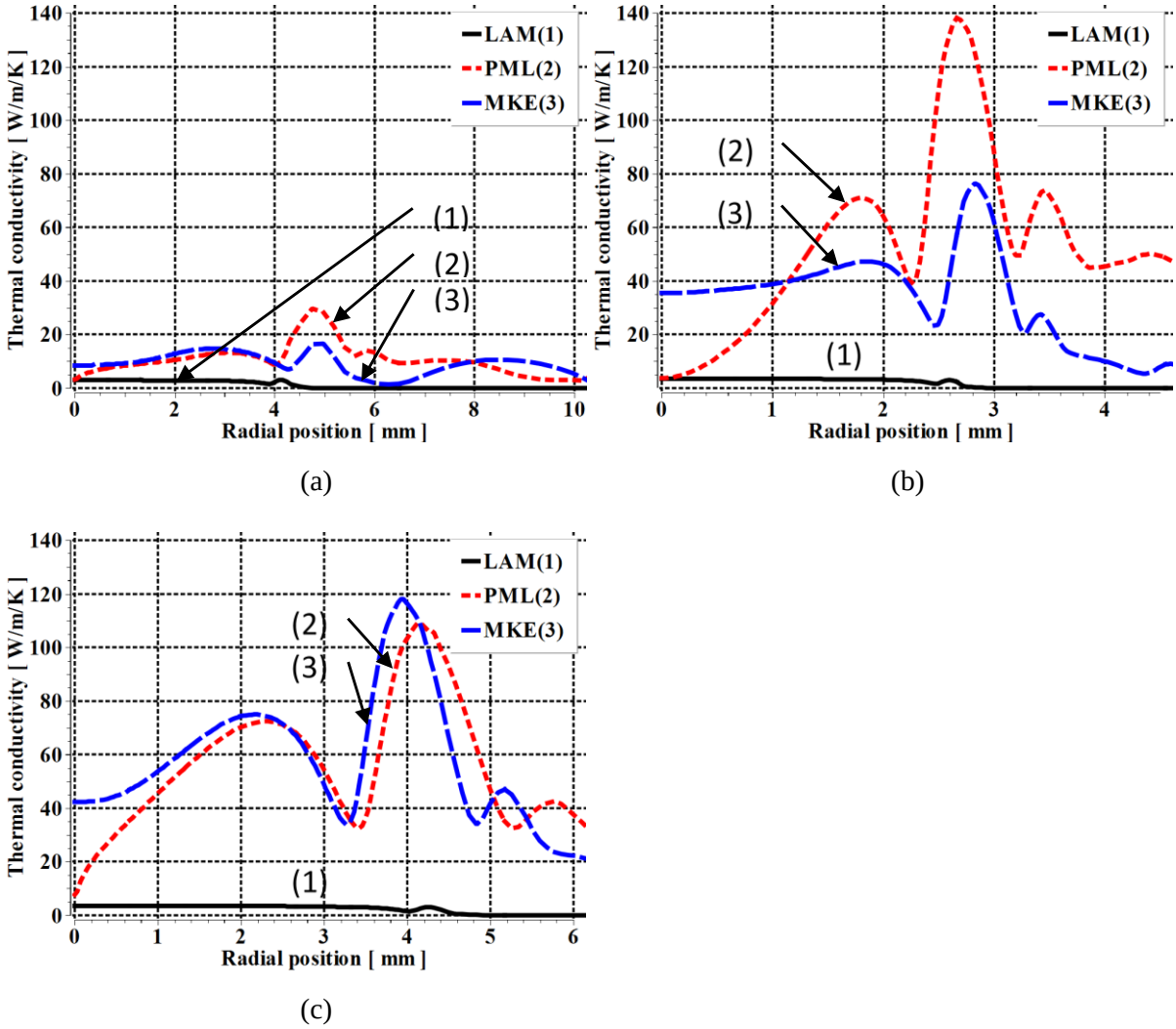

Figure 12. Radial profiles of effective thermal conductivity (sum of molecular and turbulent conductivities) computed by the three flow models for the 2 kA DC arc at P_0 = 10 bar. (a) Upstream midsection z = 15 mm, (b) Nozzle throat, z = 33 mm and (c) Downstream midsection z= 60 mm. For laminar flow, effective thermal conductivity is simply the molecular part.

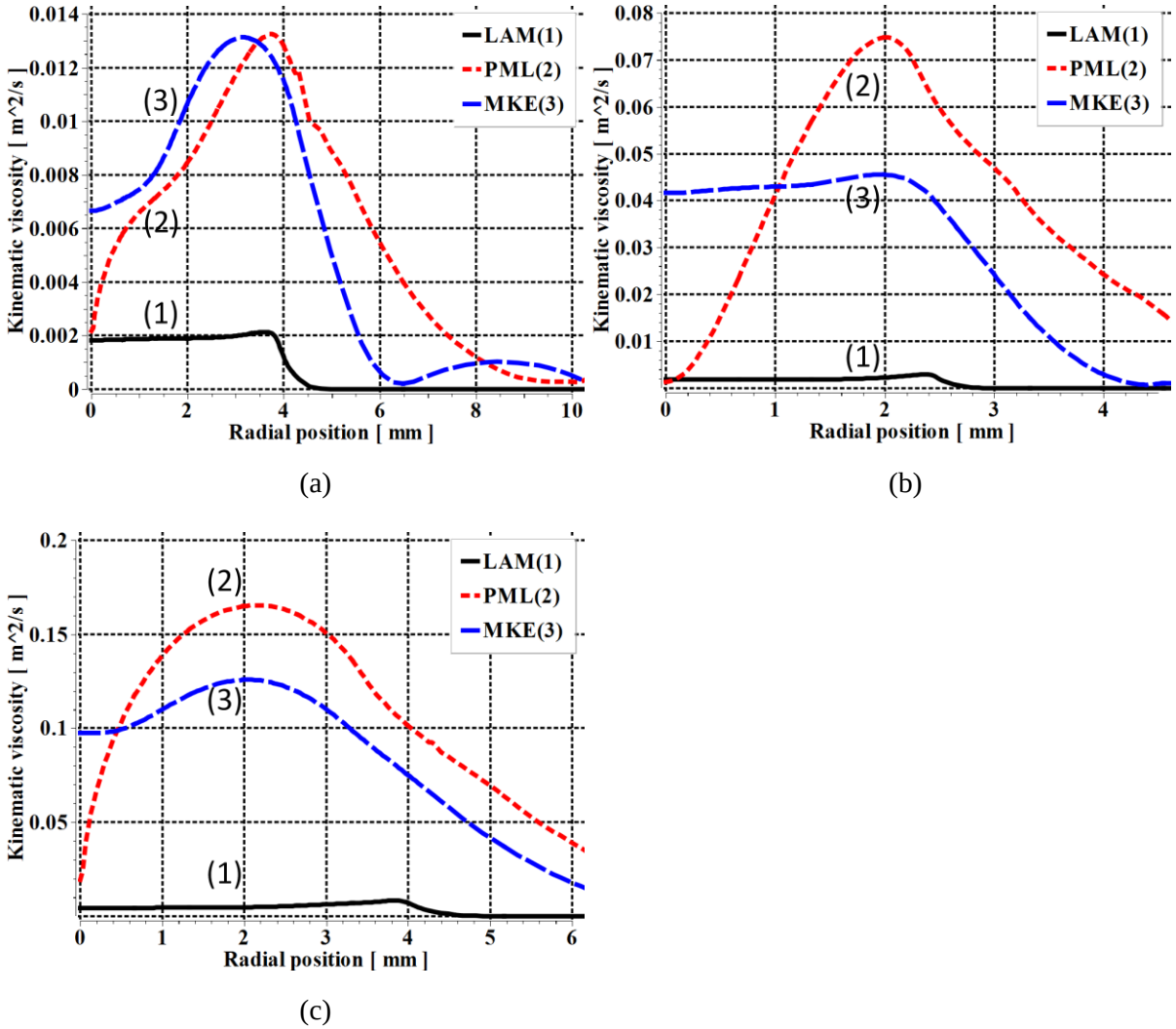

Figure 13. Radial profiles of effective kinematic viscosity (sum of molecular and turbulent kinematic viscosity) computed by the three flow models for the 2 kA DC arc at P_0 = 10 bar. (a) Upstream midsection z= 15 mm, (b) Nozzle throat, z= 33 mm and (c) downstream midsection z= 60 mm.

The peak of the effective kinematic viscosity for PML in figure 13 corresponds to the position where velocity gradient is the largest. For MKE, effective kinematic viscosity depends on k^2/ε which is more complex as this ratio is the solutions of the transport equations for k and ε, which are also closely coupled with momentum and energy conservation equations. The production of turbulence kinetic energy is related to the velocity gradients (equation (18)). Thus, for MKE the peak of effective viscosity is close to that of PML.

For both PML and MKE, the first peak of the radial profile of the effective turbulent thermal conductivity (figure 12) is associated with the peak in eddy kinematic viscosity located in the region with the largest velocity gradient. This peak is in the vicinity of 15,000K. The other two peaks at temperatures around 7000 K and 4000 K are respectively caused by the dissociation of nitrogen molecules and by that of oxygen molecules. The dissociations of nitrogen and oxygen molecules produce two peaks in the material property ρC_P as shown in figure 14. These peaks produce two inflection points on the radial temperature profile (figure 11) around 7000 K and 4000 K, respectively.

Thus, the temperature profiles for PML and MKE in the radiation re-absorption region become very broad. In the divergent section of the nozzle, there is no distinctive high temperature core. This is in contrast with the radial temperature profiles of SF_6 arc. Such broad radial temperature profile makes the arc radius very big in comparison with SF_6 arc at similar current and pressure [33]. Although there is a peak in ρC_P around 14000 K (figure 14) due to increased ionization for O^+ and N^+, its effect is less pronounced on k_t as the first peak in effective thermal conductivity in this temperature region (figure 12) is mainly produced by the radial gradient of axial velocity. In addition, in the temperature region where the first peak of the effective thermal conductivity is located, radiation transport is dominant. Thus, thermal conduction has less influence on the shape of radial temperature profile.

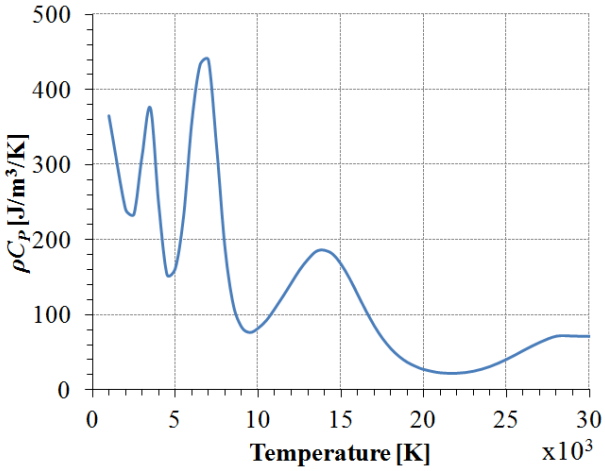

Figure 14. ρC_P of air at the pressure of 1 atm.

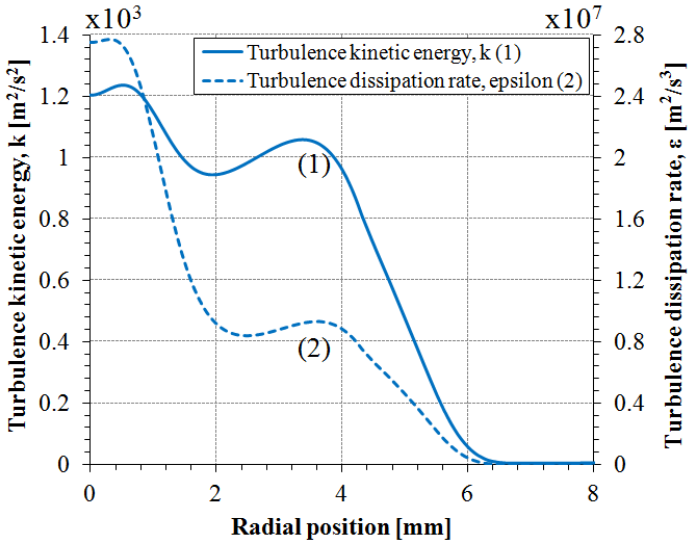

Figure 15. Radial profiles of k and ε at upstream midsection z=15 mm for the 2 kA DC arc and P_0 = 10 bar.

It should be noted that the results obtained by MKE in the upstream midsection show a local peak (figure 13(a)) in effective kinematic viscosity in the region where the temperature and axial velocity are constant (figure 11(a)). In such a region there is no mechanism for generating turbulence and k and ε should tend to zero. Numerical results of k and ε in figure 15 show that these two quantities are very small in the region for R > 6 mm. This presents much numerical difficulty in calculating the ratio of

k^2/ε accurately. However, this "artificial" peak in eddy kinematic viscosity and that in effective thermal conductivity will not affect the solutions of the governing equations in other regions as the peak occurs in a region where radial gradients of temperature and axial velocity tend to zero.

C. Energy balance

As previously indicated, temperature is determined by the balance between electrical power input and various energy transport processes as given in the energy conservation equation. The dominant energy transport processes determine the arc characteristics. It is important to identify the material properties associated with the dominant energy transport processes. The identification of such properties will serve as a basis to establish guidance for the search of a replacement gas for SF_6 as an arcing medium.

Radiation transport is an important energy transfer process in high pressure arcs. With our radiation transport model, it is natural that we examine energy balance for the arc volume up to the radial position at which the temperature is equal to 83% of the axis temperature. Following our previous work on SF_6 [33], we call this region as the arc core region although the core structure in air arc for PML and MKE is not clearly defined since outside this region temperature decay is not rapid. The energy balance for the arc core at 2 kA is given in table 2.

Table 2. Percentage of electrical power input associated with various energy transport processes for the whole arc length at the core boundary calculated by the three flow models at 2 kA and P_0 = 10 bar. Positive means power input and negative power loss.

Model	Power input (10^5 W)	Radiation loss (%)	Radial thermal conduction (%)	Axial enthalpy transport (%)	Radial enthalpy transport (%)
LAM	9.17	-72.8	-2.4	-27.7	5.8
PML	7.59	-62.5	-27.5	-2.8	-3.8
MKE	8.82	-61.3	-27.6	-3.9	-4.5

Method of calculation:

Power input = $\int_{Z1}^{Z2}\int_0^R \sigma E^2 2\pi r dr dz$

Radiation loss (%) = $-\int_{Z1}^{Z2}\int_0^R q 2\pi r dr dz$ /Power input

Radial thermal conduction (%) = $\int_{Z1}^{Z2}\int_0^R \frac{1}{r}\frac{\partial}{\partial r}\left(rk\frac{\partial T}{\partial r}\right)2\pi r dr dz$ /Power input

Axial enthalpy transport (%) = $-\int_{Z1}^{Z2}\int_0^R \rho w\frac{\partial h}{\partial z}2\pi r dr dz$ /Power input

Radial enthalpy transport (%) = $-\int_{Z1}^{Z2}\int_0^R \rho v\frac{\partial h}{\partial r}2\pi r dr dz$ /Power input

where R refers to the radial position of the core boundary or electrical boundary and ($Z2$-$Z1$) the arc length.

Conventional understanding of heat transfer by convection (hereafter referred to as enthalpy transport) is based on the non-conservative form of the energy conservation equation expressed in terms of

enthalpy [46]. Therefore, arc energy balance calculation is based on this equation. It has been found that the pressure work accounts for less than 5% of the electrical power input in all results reported in this paper. Pressure work is therefore not given in the tables related to energy balance.

It is shown in table 2 that, for the laminar flow case, the power input into the core is entirely taken out by radiation and axial enthalpy transport and 86% of the total current is carried by the core. On the other hand, radiation loss and turbulence enhanced thermal conduction account for over 90% of the power input for PML and MKE when turbulence is taken into account. The current carried by the arc core accounts for 59% of the total current for PML and 66% for MKE. It has been found that, for the two turbulence flow models (PML and MKE), on the flat part of V-I characteristics where current is larger than 2 kA, radiation loss always accounts for greater than 60% of the power input.

To assess the influence of turbulence, we need to consider the arc energy balance at the electrical boundary. This is because, between the arc core boundary and the electrical boundary, nearly 60% of the radiation flux coming out of the arc core is absorbed in this region, thus altering the energy balance. Table 3 shows how the power input into the electrically conducting core is balanced by various energy transport processes. Due to radiation absorption, the energy balance at the electrical boundary has been greatly altered in comparison with that at the core boundary. For laminar flow, radiation loss only accounts for 25% of power input while enthalpy transport (referred to as the sum of axial and radial energy transports) account for 72% of the power input with axial enthalpy transport being the dominant energy removal process and radial enthalpy an energy input mechanism. For the two turbulence models, radiation and turbulence enhanced thermal conduction account for approximately 35% power input, while enthalpy transport account for respectively 69% and 64% power input for PML and MKE, with axial enthalpy transport again being the dominant energy removal process.

Table 3. Percentage of electrical power input associated with various energy transport processes for the whole arc length at the electrical boundary calculated by various flow models at 2 kA and P_0 = 10 bar. Mathematical expressions for power input and power loss are the same as those in Table 2.

Model	Power input (10^6 W)	Radiation loss (%)	Radial thermal conduction (%)	Axial enthalpy transport (%)	Radial enthalpy transport (%)
LAM	1.07	-25.1	-1.6	-106.9	35.3
PML	1.29	-14.7	-19.7	-85.1	16.6
MKE	1.33	-16.3	-21.7	-61.3	-2.5

Although turbulence enhanced thermal conduction is not dominant at the electric boundary, it redistributes the energy inside the arc's thermal influence region, thus giving rise to very broad radial temperature profile, which in turn enhances enthalpy transport. Such behaviour is reflected in the results of Table II, which indicates that power loss by enthalpy transport for the arc in turbulent flow (8.8×10^4 W for PML and 8.5×10^4 W for MKE) is higher than that in the laminar flow (7.7×10^4 W). The enhanced enthalpy transport due to the broad radial temperature profile together with turbulent thermal conduction results in a 20% increase in arc voltage compared with that of LAM. This is in contrast with arcs in SF_6 for which turbulence effects have little influence on arc voltage [33].

4.2.3 Characteristics of nozzle air arc with radiation and thermal conduction dominated high temperature core

When current is reduced from 2 kA, the relative importance of radiation as an energy loss mechanism is reduced while thermal conduction gradually becomes the dominant energy transport process for arcs in turbulent flow. Arc area reduces at a faster rate than current and arc voltage increases with decreasing current for turbulent arcs. However, for arcs in laminar flow, radiation is still the dominant energy removal process and the arc area is still approximately proportional to current. Arc voltage of the laminar flow arc is hardly increased when the current is reduced to 250 A (figure 8).

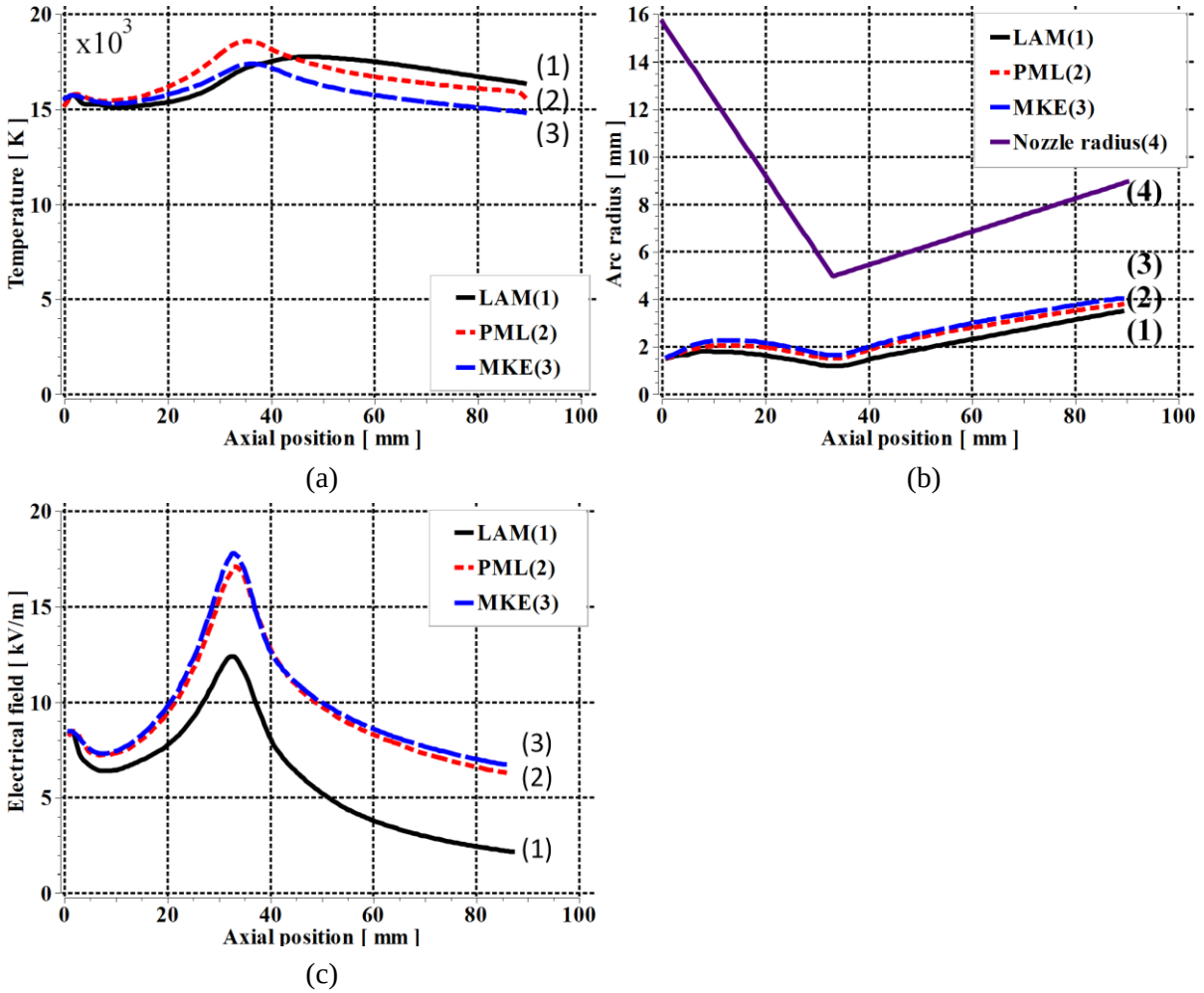

Figure 16. Variations of (a) temperature (b) arc radius and (c) electric field along the nozzle axis for the 250 A DC arc at P_0 = 10 bar computed by the three flow models.

The qualitative features of axis temperature (figure 16(a)), arc radius (figure 16(b)) and electric field (figure 16(c)) distributions of the arc at 250 A are similar to those of at 2 kA. Arc radius is the smallest for the laminar flow arc but its temperature downstream of throat is the highest. The axis temperature for PML is higher than that for MKE but the latter has a larger arc radius. This results in the electric field for MKE being slightly higher than that for PML (figure 16(c)). There is only 3.5% difference in arc voltages predicted by these two turbulence models. Radial temperature profiles at three axial stations for the three flow models are given in figure 17. The features of radial temperature profiles at 250 A are similar to those at 2 kA (figures 11 and 17). However, the relative size of the thickness of the

radiation re-absorption region to the arc core size is increased compared with that of the 2 kA arc, especially in the downstream region of the throat (figure 17(c)). Such a broad temperature profile at low currents will have detrimental effects for arc thermal extinction during the current zero period. The peaks of effective thermal conductivity at 7000 K and 4000 K are again responsible for such broad radial temperature profiles.

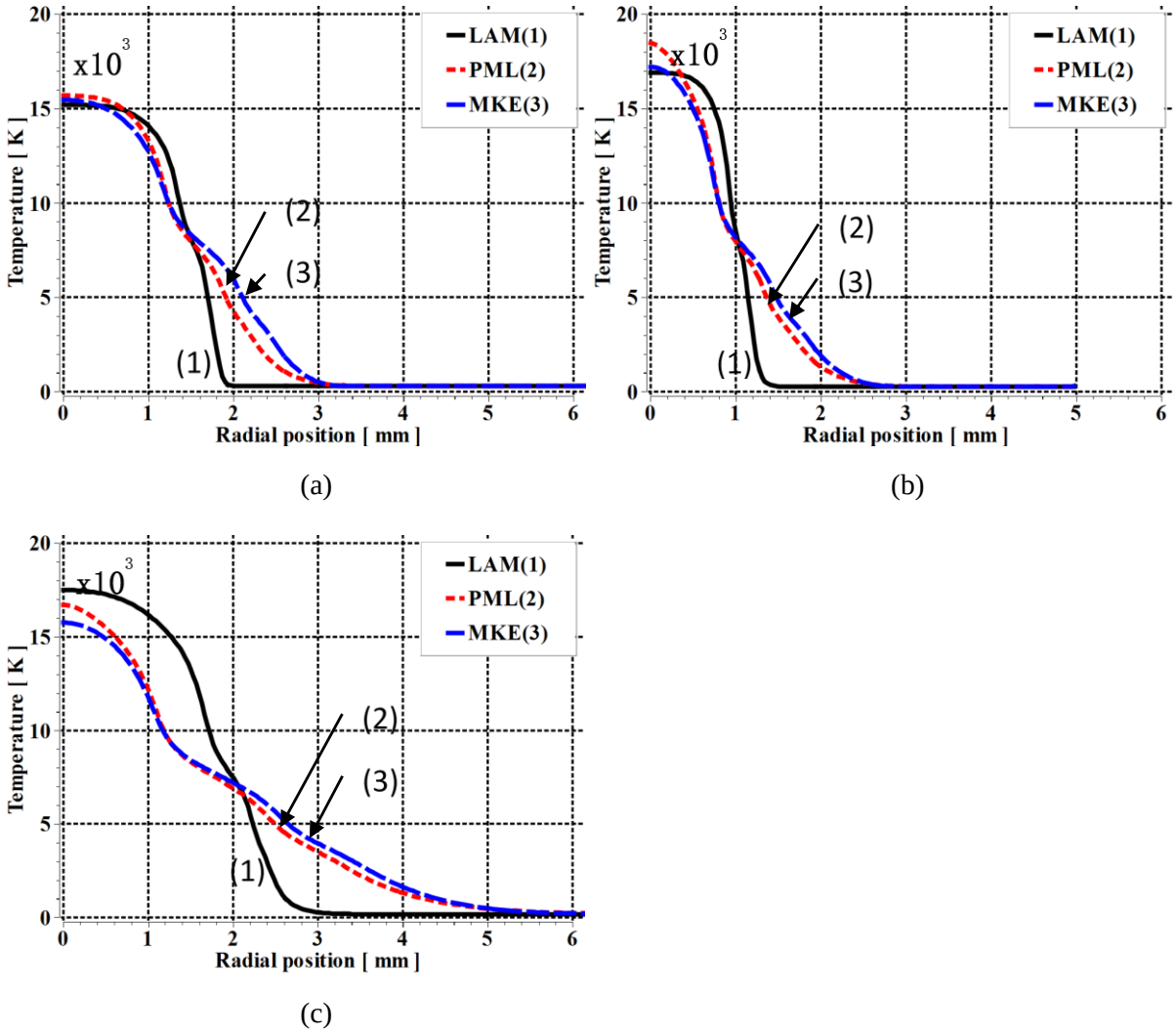

Figure 17. Radial temperature profiles computed by the three flow models for the 250 A DC arc at P_0 = 10 bar. (a) Upstream midsection, z= 15 mm, (b) Nozzle throat, z= 33 mm and (c) Downstream midsection z= 60 mm.

Energy balance calculation at 250 A indicates that, for the laminar flow model, at the core boundary, radiation is still dominant. For PML and MKE, turbulence enhanced thermal conduction becomes dominant with radiation accounting respectively for 36% and 26% of the power input (table 4). At the electric boundary (table 5), for the laminar flow model, enthalpy transport together with radiation loss account for 84% of the power input. For the two turbulence models, turbulence enhanced thermal conduction and enthalpy transport account for 90% of the power input with thermal conduction the most important energy transport process. Similar to the arc at high currents, turbulence enhanced thermal conduction gives rise to very broad radial temperature profile, which further enhances enthalpy transport. The dominance of turbulence effects at low currents, together with the turbulence

enhanced enthalpy transport through the broad radial temperature profile, is responsible for the rapid rising arc voltage with decreasing current.

Table 4. Percentage of electrical power input associated with various energy transport processes for the whole arc length at the core boundary calculated by the three flow models at 250 A and P_0 = 10 bar. Mathematical expressions for power input and power loss are the same as those in Table 2.

Model	Power input (10^5 W)	Radiation loss (%)	Radial thermal conduction (%)	Axial enthalpy transport (%)	Radial enthalpy transport (%)
LAM	1.12	-64.6	-15.3	-25.2	7.6
PML	1.29	-35.9	-63.2	2.8	-2.5
MKE	1.35	-26.4	-70.0	0.9	-1.6

Table 5. Percentage of electrical power input associated with various energy transport processes for the whole arc length at the electrical boundary calculated by the three flow models at 250 A and P_0 = 10 bar. Mathematical expressions for power input and power loss are the same as those in Table 2.

Model	Power input (10^5 W)	Radiation loss (%)	Radial thermal conduction (%)	Axial enthalpy transport (%)	Radial enthalpy transport (%)
LAM	1.39	-20.8	-7.8	-134.1	65.5
PML	2.27	-8.2	-54.8	-45.5	9.9
MKE	2.34	-6.1	-54.6	-49.0	11.1

4.2.4 The effects of stagnation pressure

Computation of arc voltage has also been done using PML and MKE for P_0 = 7 bar and 13 bar. The laminar flow model is not used as it cannot give a satisfactory account of energy loss mechanism. Qualitative arc features at P_0 = 7 bar and 13 bar are similar to the arc at P_0 = 10 bar. Table 6 summarizes the arc voltages computed for the three pressures together with the corresponding experimental results, which were given in [5].

Computations have only been done for those cases where experimental results are available for comparison with the predicted voltage. For P_0 = 7 bar, the arc in the divergent section near the nozzle exit already fills the nozzle for currents around 2 kA, which renders the adiabatic boundary condition invalid. Thus, no computational results are given for currents above 2 kA at P_0 = 7 bar. The experimental results given in Table 6 (referred to as Exp in the table) are derived from the non-dimensional V-I characteristics of [5] which are subject to an error of $\pm$10% around the value given in table 6.

Table 6. Arc voltages by the three flow models for different values of P_0 and the currents ranging from 250 A to 3 kA.

U(V)	**P_0 = 13 bar**		
I (A)	**PML**	**MKE**	**Exp**
1000	876	1071	1075
1500		937	924
2000	760	846	848
2500		777	803
3000	696	715	773
U(V)	**P_0 = 10 bar**		
I (A)	**PML**	**MKE**	**Exp**
250	906	937	930
500	830	842	850
1000	754	746	750
1500	690	677	700
2000	645	665	650
2500	630	650	650
3000	622	648	660
U(V)	**P_0 = 7 bar**		
I (A)	**PML**	**MKE**	**Exp**
500	688	737	789
1000	612	636	667
1500		588	626
2000	533	552	606

Table 6 indicates that voltages predicted by PML and MKE at P_0 = 10 bar fall within the error bar (figure 8). That means that there is no preference as regards which turbulence model should be used for P_0 = 10 bar. However, arc voltage predicted by MKE for P_0 = 7 bar and 13 bar is closer to the experimental results than that by PML. This indicates that MKE gives a better description of the length and velocity scales of the eddies responsible for turbulent energy transfer at P_0 = 7 and 13 bar. For the accuracy of prediction under a wide range of gas discharge conditions, MKE is a preferred turbulence model for air nozzle arcs although computational cost is higher than that of PML.

If we use the voltages predicted by MKE at P_0 = 10 bar as the base to investigate the pressure dependence of voltage, we find that the voltages at P_0 = 13 bar are proportional to the stagnation pressure to the power of 1.2 and those for P_0 = 7 bar to the power of 0.4. This is in contrast with the voltage of DC SF_6 arcs which is proportional to the square root of stagnation pressure [33]. For air nozzle arc it appears that there is no simple relationship between arc voltage and stagnation pressure. However, this could be a direct consequence of an arc burning in a very narrow divergent section of the nozzle. When current is sufficiently high for a given stagnation pressure (for example at 2 kA and P_0 = 7 bar), the arc in this section is no longer surrounded by a cold flow as in the case for SF_6 nozzle arc [33].

4.3 Implication on SF_6 replacement

It has been known that the excellent thermal interruption capability of SF_6 gas attributes to the turbulent effect that enhances energy transport during the current zero period [47]. In the present work, we have firmly established that turbulence is operating in air nozzle arcs. Experimental studies [12] have however shown that the interruption capability of air is only one-third of that of SF_6. The question that naturally follows is why turbulence plays a more significant part in arc cooling in the case of SF_6 being the interruption gas. The present work provides vital information for an explanation.

Previous studies on detailed energy balance [33] have shown that in terms of the energy loss mechanisms close to the current zero point, turbulence enhanced radial conduction dominates the cooling process. When turbulence operates in low current SF_6 nozzle arc, radial thermal conduction and radiation practically takes all the electrical power input out of the arc column. SF_6 nozzle arc has a clear and narrow core structure. In air, turbulence leads however to a very different scenario. Turbulence broadens the air arc column with a less clearly definable arc core and subsequently leads to changes in the contributions by radial and axial energy transport towards the overall energy balance. The changes are expected to be significant at lower current in both steady and transient cases, and thus adversely affect the interruption capability of air.

It is the peaks in ρC_P as a function of temperature that leads to the broadening of the arc column in air. It is the first time that we are able to trace the different behaviors of SF_6 and air arcs to the differences in material properties. To have a gas with excellent interruption capability, there should be as large as possible a value of ρC_P immediately below the conducting temperature of the gas (usually around 4000 K, figure 18) and have ideally no peaks of ρC_P above this conducting temperature. This ensures small effective thermal conductivity, k_t, for temperature above 4000 K. For a given thermal flux per unit area, a small k_t requires a large radial temperature gradient, thus creating a rapidly decaying temperature region above 4000 K. The presence of a peak in ρC_P below 4000 K produces a peak in k_t which requires a much smaller radial temperature gradient for the same thermal flux per unit area coming from the region where temperature is above 4000 K, thus producing the tail of a radial temperature profile. This mechanism is responsible for the formation of a distinctive SF_6 arc core. Since CO_2 is a gas which is extensively investigated as a candidate for replacing SF_6, its ρC_P is also given in figure 18. If turbulence is important in CO_2 nozzle arcs, the shape of its radial temperature profile is expected to be similar to that of air nozzle arc due to the two peaks in ρC_P occur close to the two of the air. This implies inferior thermal interruption capability of CO_2 to that of SF_6.

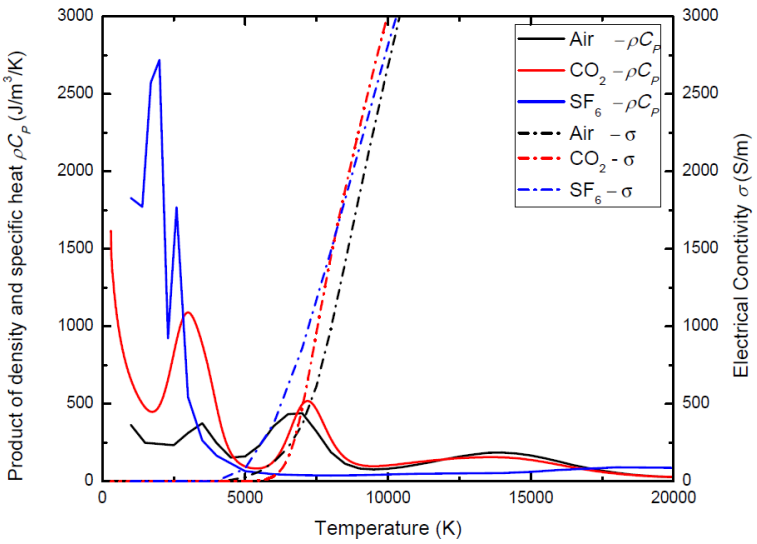

Figure 18. Electrical conductivity σ and ρC_P of SF_6 [48], CO_2 [49] and air [13] at the pressure of 1 atm.

5 Conclusions

A detailed computational investigation into the behaviour of an air arc burning in the nozzle of Fang et al [5] has been carried out using three flow models, the laminar flow model, the Prandtl mixing length model (PML) and the modified k-epsilon model (MKE). Arc voltage predicted by the laminar flow arc model is considerably lower than the measured arc voltage while the standard k-epsilon model grossly over predicts the arc voltage in comparison with experimental results. A modified k-epsilon turbulence model is then introduced to reduce the turbulence effects by adjusting one of the five turbulence parameters ($C_{1\varepsilon}$) to increase the turbulence dissipation rate. The value of $C_{1\varepsilon}$ and that of the turbulence parameter in PML, c, have been found respectively to be 1.62 and 0.06 by matching the predicted arc voltage with that measured arc voltage at 1 kA and P_0 = 10 bar. These values have been used by PML and MKE to predict the arc voltage at other current and stagnation pressure.

When the dominant energy transport is radiation loss at the arc core boundary, arc voltage is almost independent of the current for all flow models. This is the case for currents no less than 2 kA. Turbulent enhanced thermal conduction through the influence of the peaks in ρC_P results in very broad radial temperature profile. This in turn enhances axial enthalpy transport, which, together with turbulent thermal conduction, increases arc power loss by 20% in comparison with that of LAM at the same current. Thus, turbulence is important at high currents.

For PML and MKE when current is reduced from 2 kA at P_0 = 10 bar arc voltage starts to rise. At the arc core boundary, thermal conduction gradually becomes the dominant energy transport process. At the electrical boundary, thermal conduction and enthalpy transport balance the power input with thermal conduction being the dominant energy loss mechanism.

Qualitative arc features at different stagnation pressures are similar. There is no simple relationship between arc voltage and stagnation pressure for the nozzle of [5]. This is probably the consequence of a narrow divergent section after the throat. Overall, MKE gives the best agreement with experimentally measured arc voltage for the three stagnation pressures investigated. Therefore, MKE

is the preferred arc model for air nozzle arcs.

A distinct feature of air arcs is the shape of its radial temperature profile. For air arcs under turbulent flow there is no distinctive high temperature core. Radial temperature profile is very broad with the thickness of the radiation re-absorption region bigger than the core. The radial extent of the arc's thermal influence region for air arcs is much bigger than SF_6 under similar discharge conditions. Such broad radial temperature profile is due to the material property of air, ρC_P, which is responsible for the peaks in turbulent thermal conductivity at 4000 K and 7000 K due to respectively the dissociation of oxygen molecules and nitrogen molecules. Such peaks will have detrimental effects on arc's thermal recovery. To seek replacement gas for SF_6, one should aim at finding a gas whose ρC_P does not have peaks above 4000 K at which electrical conductivity due to thermal ionization is negligible. Yet, a peak in ρC_P is desirable just below 4000 K. This will results in a radial temperature profile with very rapid temperature decay above 4,000 K and a gentle temperature tail below 4000 K. This ensures a core formation and a small arc size. ρC_P of SF_6 has such properties, hence superior arc quenching capability. In addition to the consideration of arc interruption capability, a replacement gas for SF_6 should have comparable dielectric strength to that of SF_6. This aspect is beyond the scope of the current investigation.

References

[1] Christophorou L G, Olthoff J K and Green D S 1997 Gases for electrical insulation and arc interruption:possible present and future alternatives to SF_6 NIST Technical Note 1425, US Department of Commerce

[2] Flurscheim C H 1982 Power circuit breaker theory and design (revised edition) (London, UK: Peter Peregrinus Ltd.)

[3] Bothwell I R, Cowley M D and Grycz B 1974 High current D.C. arc in uniform flow *Proc. 3rd Int. Conf. on Gas Discharges and Their Applications IEE* vol 118 pp 493-7

[4] Malghan V R, Fang M T C and Jones G R, 1977 Investigation of quasi-steady-state high-current arcs in an orifice air flow *J. Appl. Phys.* **48**(6) 2331-7

[5] Fang M T C, Ramakrishnan S and Messerle H K 1980 Scaling laws for gas-blast circuit-breaker arcs during the high current phase *IEEE Trans. Plasma Sci.* **PS-8** 357-62

[6] Frind G and Rich J A 1974 Recovery speed of axial flow gas blast interrupter: dependence on pressure and di/dt for air and SF_6 *IEEE Trans. Power Appar. Syst.* **93** 1675-84

[7] Cowley M D 1974 Integral methods of analysing electric arcs: I. Formulation *J. Phys. D: Appl. Phys.* **7** 2218-31

[8] Cowley M D and Chan S K 1974 Integral methods of analysing electric arcs: II. Examples *J. Phys. D: Appl. Phys.* **7** 2232-45

[9] Chan S K, Cowley M D and Fang M T C 1976 Integeral method of arc analysis: III. Shape-factor correlation for low radiation and laminar flow *J. Phys. D: Appl. Phys.* **9** 1085-99

[10] Zhang J F, Fang M T C and Newland D B 1987 Theoretical investigation of a 2 kA arc in a supersonic nozzle *J. Phys. D: Appl. Phys.* **20** 368-79

[11] Fang M T C and Lin W Y 1990 Current zero behaviour of gas-blast arc, Pt I: Nitrogen *IEE. Proc. A.* **137**(4) 175-83

[12] Stoller P C, Seeger M, Iordanidis A A and Naidis G V 2013 CO_2 as an arc interruption medium in gas circuit breakers *IEEE Trans. Plasma Sci.* **41**(8) 2359-69

[13] Yos J M 1967 Transport properties of Nitrogen, Hydrogen, Oxygen and Air to 30000K (Washington D C: Research and Advanced Development Division Corporation)
[14] Devoto R S 1976 Electron transport properties in high-temperature air *Phys of Fluids.* **19** 22-4
[15] Murphy A B 1995 Transport Coefficients of Air, Argon-Air, Nitrogen-Air, and Oxygen-Air Plasma *Plasma Chemistry and Plasma Processing* 15(2) 279-307
[16] Capitelli M, Colonna G, Gorse C and D'Angola A 2000 Transport properties of high temperature air in local thermodynamic equilibrium *Eur. Phys. J. D.* **11** 279-89
[17] Cressault Y, Hannachi R, Teulet Ph, Gleizes A, Gonnet J-P and Battandier J-Y 2008 Influence of metallic vapours on the properties of air thermal plasmas *Plasma Sources Sci. Technol.* **17** 035016
[18] Cressault Y, Gleizes A and Riquel G 2012 Properties of air–aluminum thermal plasmas *J. Phys. D: Appl. Phys.* **45** 265202
[19] Wang W Z, Wu Y, Rong M Z and Yang F 2012 Theoretical computation studies for transport properties of air plasmas Acta. Physica. Sinica. **61**(10) 105201 (in Chinese)
[20] Asinovsky E I, Kirillin A V, Pakhomov E P and Shabaskov V E 1971 Experimental investigation of transport properties of low-temperature plasma by means of electric arc *Proceedings of the IEEE*. **59**(4) 592-601
[21] Schreiber P W, Hunter A M and Benedetto K R 1973 Electrical conductivity and total emission coefficient of air plasma *AIAA Journal.* **11**(6) 815-21
[22] Liu J 2016 Modelling and simulation of air and SF_6 switching arcs in high voltage circuit breakers (PhD Thesis: University of Liverpool, Liverpool)
[23] Fang M T C, Fung H and Edels H 1973 A.C.-Arc-column and current-zero properties *Proc IEE.* **120** 709-14
[24] Yan J D 1997 Investigation of electric arcs in self-generated flow (PhD Thesis: University of Liverpool, Liverpool)
[25] Aubrecht V and Bartlova M 2008 Radiation transfer in thermal plasmas of air, N_2 and CO_2 *Proc. 17th Int. Conf. on Gas Discharges and Their Applications (Cardiff)* pp 393-6
[26] Aubrecht V and Bartlova M 2009 Net emission coefficients of radiation in air and SF_6 thermal plasmas *Plasma Chem. Plasma. Process.* **29** 131-47
[27] Billoux T, Cressault Y, Teulet P and Gleizes A 2012 Calculation of the net emission coefficient of an air thermal plasma at very high pressure *12th High-Tech Plasma Processes Conference (HTPP-12), J. Phys. Conference Series* **406** 012010
[28] Naghizadeh-Kashani Y, Cressault Y and Gleizes A 2002 Net emission coefficient of air thermal plasmas *J. Phys. D: Appl. Phys.* **35** 2925-34
[29] Peyrou B, Chermartin L, Lalande P, Cheron B G, Riviere P, Perrin M Y and Soufiani A 2012 Radiative properties and radiative transfer in high pressure thermal air plasmas *J. Phys. D: Appl. Phys.* **45** 455203
[30] Gleizes A, Rahmani B, Gonzalez J J and Liani B 1991 Calculation of net emission coefficient in N_2, SF_6 and SF_6-N_2 arc plasmas *J. Phys. D: Appl. Phys.* **24** 1300-9
[31] Ernst K A, Kopainsky J G and Maecker H H 1973 The energy transport, including emission and absorption, in N_2-arcs of different radii *IEEE Trans. Plasma Sci.* **1**(4) 3-16
[32] Shayler P J and Fang M T C 1978 Radiation transport in wall-stabilised nitrogen arcs *J. Phys. D: Appl. Phys.* **11** 1743-56
[33] Zhang Q, Yan J D and Fang M T C 2014 The modelling of an SF_6 arc in a supersonic nozzle: I. Cold flow features and dc arc characteristics *J. Phys. D: Appl. Phys.* **47** 215201

[34] Walmsley H J, Gone G R, Haji F and Strachan D C 1977 Core fluctuations of gas-blast circuit-breaker arc *J. Phys. D: Appl. Phys.* **10** 383-92
[35] Schlichting H 1979 Boundary Layer Theory 7th edn (New York: McGraw Hill)
[36] Launder B E and Spalding D B 1972 Mathematical models of turbulence (London and New York: Academic Press)
[37] Wilcox D C 2006 Turbulence Modeling for CFD (La Cañada, CA: DCW Industries)
[38] Zhang Q, Yan J D and Fang M T C 2016 The modelling of an SF_6 arc in a supersonic nozzle: II. Current zero behaviour of the nozzle arc *J. Phys. D: Appl. Phys.* **49** 335501
[39] ANSYS Fluent is the name of a commercial CFD package supplied by ANSYS which is based at Southpointe, 2600 ANSYS Drive, Canonsburg, PA 15317, USA.
[40] Gonzaliez J J, Gleizes A and Kerenek P 1994 SF_6 circuit breaker arc modelling: influence of the electric field on the electrical conductivity *J. Phys. D: Appl. Phys.* **27** 985-93
[41] Belhaouari J B, Gonzalez J J and Gleizes A 1998 Simulation of a decaying SF_6 arc plasma: Hydrodynamic and kinetic coupling *J. Phys. D: Appl. Phys.* **31** 1219- 32
[42] Gonzalez J J, Girard R and Gleizes A 2000 Decay and post-arc phases of a SF_6 arc plasma: a thermal and chemical non-equilibrium model *J. Phys. D: Appl. Phys.* **33** 2759- 68
[43] Poinsot T and Veynante D 2005 Theoretical and Numerical Combustion 2nd edn (Philadelphia: Edwards)
[44] Davidson P A 2004 Turbulence: An Introduction for Scientists and Engineers (Oxford: Oxford University Press)
[45] Fang M T C and Newland D B 1983 DC nozzle arcs with mild wall ablation *J. Phys. D: Appl. Phys.* **16**(5) 793-810
[46] Anderson J D1982 Modern Compressible Flow (New York: McGraw-Hill)
[47] Fang M T C, Zhuang Q and Guo X J 1994 Current zero behaviour of an SF_6 gas-blast arc Part II: turbulent flow *J. Phys. D: Appl. Phys.* **27** 74-83
[48] Frost L S and Liebermann R W 1971 Composition and transport properties of SF_6 and their use in a simplified enthalpy flow arc model *Proc. IEEE.* **59** 474-85
[49] Matsumura T, Yokomizu Y, Kondo T, Uchii T, Kawano H and Suzuki K 2009 Thermodynamic and transport properties of CO_2 admixed with N_2 at temperatures of 300-30,000 K *Proc. of the 7th Int. Symp. on Applied Plasma Science (Hamburg, Germany)* pp 59-62